2540 *Chem. Mater.* **2009,** *21,* 2540–2546

Mesoporous Monocrystalline TiO_2 and Its Solid-State Electrochemical Properties

Wenbo Yue,[†] Xiaoxiang Xu,[†] John T. S. Irvine,[†] Pierrot S. Attidekou,[†] Chong Liu,[‡]
Heyong He,[‡] Dongyuan Zhao,[‡] and Wuzong Zhou*[,†]

*School of Chemistry, University of St. Andrews, St. Andrews, Fife KY16 9ST, United Kingdom, and
Department of Chemistry, Fudan University, Shanghai 200433, China*

Received January 21, 2009. Revised Manuscript Received April 6, 2009

Mesoporous monocrystalline rutile TiO_2 has been fabricated at low temperature using mesoporous silicas SBA-15 and KIT-6 as hard templates. The key step of the synthetic process was introducing titanium nitrate complex into the template pores and allowing it to dry, dehydrate, decompose, and finally, form TiO_2 crystals in the pores. It was found that the reaction temperature and concentration of HNO_3 in the used precursor had great effects to the crystallization of TiO_2. Removal of the silica templates after the TiO_2 crystallization has been investigated. Crystallization of TiO_2 in cage-containing mesoporous silicas, FDU-12 and SBA-16 was not successful, further confirming the previous speculation about strong interaction between the crystals and the wall of silica cages. The porous titanium oxide specimens were characterized by using various techniques, including XRD, HRTEM, and nitrogen adsorption/desorption. Proton conductivity and Li-ion insertion property of the samples were also examined. The highest conductivity, 8×10^{-3} S cm^{-1}, was obtained at 50 °C under 100% RH and 1 Li^+ could be accommodated per TiO_2 unit (335 mA h/g) for the first discharge.

Introduction

Ordered mesoporous oxides have a wide range of potential applications in catalysis, nanoreactors, electronic devices, energy storage, and gas sensors because of their large surface areas, large pore volumes and ordered pore networks.[1] Since the first ordered mesoporous silica, MCM-41,[2] was synthesized based on deposition of silica precursor on the surface of micelles of surfactants in 1990s, similar methods have been used to synthesize various porous metal oxides (e.g., TiO_2 and ZrO_2).[3] However, these mesoporous metal oxides synthesized using surfactants (P123, F127, etc.) as templates are normally noncrystalline because the soft templates cannot tolerate the high temperature required for crystallization of metal oxides. On the other hand, porous monocrystalline transition metal oxides can be obtained using hard templates such as mesoporous silicas, SBA-15,[4] KIT-6,[5] FDU-12,[6] SBA-16,[7] or mesoporous carbon, CMK-3.[8] For example, porous crystals of Co_3O_4, In_2O_3, NiO, CeO_2, Mn_2O_3, Cr_2O_3, WO_3, Fe_2O_3 and MnO_2[9,10] templated by SBA-15 and KIT-6 have been synthesized using the evaporation method[11] or the solid−liquid method.[12] Among these porous oxides, only cubic oxides such as Co_3O_4 and In_2O_3 have been templated by cage-containing FDU-12 and SBA-16. The possible influence factors were brought forward in our previous work as strong interactions between the crystals and walls of the cages.[13] The expected morphologies of these porous oxides should be similar to the shapes of the pore networks in the

---

* Corresponding author. E-mail: wzhou@st-andrews.ac.uk.

[†] University of St. Andrews.

[‡] Fudan University.

(1) (a) Sano, T.; Oumi, Y. *Catal. Surv. Asia* **2004**, *8*, 295–304. (b) Nelson, P. A.; Owen, J. R. *J. Electrochem. Soc.* **2003**, *150*, A1313−A1317. (c) Hyodo, T.; Shimizu, Y.; Egashira, M. *Electrochem.* **2003**, *71*, 387–393. (d) Mehandjiev, D.; Nikolovazhecheva, E. *J. Catal.* **1980**, *65*, 475–477. (e) Miao, S. J.; Deng, Y. Q. *Appl. Catal. B: Environ.* **2001**, *31*, L1−L4. (f) Danks, M. J.; Jervis, H. B.; Nowotny, M.; Zhou, W. Z.; Maschmeyer, T. A.; Bruce, D. W. *Catal. Lett.* **2002**, *82*, 95–98. (g) King, N. C.; Dickinson, C.; Zhou, W. Z.; Bruce, D. W. *Dalton Trans.* **2005**, 1027–1032.

(2) Kresge, C. T.; Leonowicz, M. E.; Roth, W. J.; Vartuli, J. C.; Beck, J. S. *Nature* **1992**, *359*, 710–712.

(3) (a) Attard, G. S.; Goltner, C. G.; Corker, J. M.; Henke, S.; Templer, R. H. *Angew. Chem., Int. Ed.* **1997**, *36*, 1315–1317. (b) Antonelli, D. M.; Ying, J. Y. *Angew. Chem., Int. Ed.* **1995**, *34*, 2014–2017. (c) Ciesla, U.; Schacht, S.; Stucky, G. D.; Unger, K. K.; Schuth, F. *Angew. Chem., Int. Ed.* **1996**, *35*, 541–543. (d) Yang, P. D.; Zhao, D. Y.; Margolese, D. I.; Chmelka, B. F.; Stucky, G. D. *Nature* **1998**, *396*, 152–155. (e) Tian, B. Z.; Liu, X. Y.; Tu, B.; Yu, C. Z.; Fan, J.; Wang, L. M.; Xie, S. H.; Stucky, G. D.; Zhao, D. Y. *Nat. Mater.* **2003**, *2*, 159–163.

(4) Zhao, D. Y.; Feng, J. L.; Huo, Q. S.; Melosh, N.; Fredrickson, G. H.; Chmelka, B. F.; Stucky, G. D. *Science* **1998**, *279*, 548–552.

(5) Kleitz, F.; Choi, S. H.; Ryoo, R. *Chem. Commun.* **2003**, 2136–2137.

(6) (a) Fan, J.; Yu, C. Z.; Gao, F.; Lei, J.; Tian, B. Z.; Wang, L. M.; Luo, Q.; Tu, B.; Zhou, W. Z.; Zhao, D. Y. *Angew. Chem., Int. Ed.* **2003**, *42*, 3146–3150. (b) Fan, J.; Yu, C. Z.; Lei, J.; Tu, B.; Zhang, Q.; Zhou, W. Z.; Zhao, D. Y. *J. Am. Chem. Soc.* **2005**, *127*, 10794–10795.

(7) Zhao, D. Y.; Huo, Q. S.; Feng, J. L.; Chmelka, B. F.; Stucky, G. D. *J. Am. Chem. Soc.* **1998**, *120*, 6024–6036.

(8) Jun, S.; Joo, S. H.; Ryoo, R.; Kruk, M.; Jaroniec, M.; Liu, Z.; Ohsuna, T.; Terasaki, O. *J. Am. Chem. Soc.* **2000**, *122*, 10712–10713.

(9) Dickinson, C.; Zhou, W. Z.; Hodgkins, R. P.; Shi, Y. F.; Zhao, D. Y.; He, H. Y. *Chem. Mater.* **2006**, *18*, 3088–3095.

(10) (a) Zhu, K. K.; Yue, B.; Zhou, W. Z.; He, H. Y. *Chem. Commun.* **2003**, 98–99. (b) Jiao, F.; Harrison, A.; Jumas, J. C.; Chadwick, A. V.; Kockelmann, W.; Bruce, P. G. *J. Am. Chem. Soc.* **2006**, *128*, 5468–5474. (c) Jiao, F.; Jumas, J. C.; Womes, M.; Chadwick, A. V.; Harrison, A.; Bruce, P. G. *J. Am. Chem. Soc.* **2006**, *128*, 12905–12909. (d) Jiao, F.; Bruce, P. G. *Adv. Mater.* **2007**, *19*, 657–660. (e) Yue, B.; Tang, H. L.; Kong, Z. P.; Zhu, K. K.; Dickinson, C.; Zhou, W. Z.; He, H. Y. *Chem. Phys. Lett.* **2005**, *407*, 83–86. (f) Jiao, K.; Zhang, B.; Yue, B.; Ren, Y.; Liu, S.; Yan, S.; Dickinson, C.; Zhou, W. Z.; He, H. Y. *Chem. Commun.* **2005**, 5618–5120.

(11) Tian, B. Z.; Liu, X. Y.; Yang, H. F.; Xie, S. H.; Yu, C. Z.; Tu, B.; Zhao, D. Y. *Adv. Mater.* **2003**, *15*, 1370–1374.

(12) Yue, W. B.; Zhou, W. Z. *Chem. Mater.* **2007**, *19*, 2359–2363.

10.1021/cm900197p CCC: $40.75

templates (see the Supporting Information, Figure S1). In other words, the porous oxides are negative replicas of the silica templates. However, to date, there is no report about the synthesis of mesoporous monocrystalline TiO_2, although TiO_2 has been proven to be an excellent photocatalyst, electrode, and gas sensor based on its unique electronic and optical properties.[14]

In the realm of electrochemistry, titanium oxides show a phase dependent diverse lithium insertion chemistry.[15] The spinel, $Li_4Ti_5O_{12}$, reversibly accepts three Li^+ cations per formula unit with a two phase equilibrium for 180 or 190 mA h/g insertion at 1.53 V, as $Li_7Ti_5O_{12}$ and $Li_4Ti_5O_{12}$[16] have essentially the same lattice parameter, yielding excellent reversibility. The ramsdellite solid solution based upon $Li_2Ti_3O_7$ and $LiTi_2O_4$[17] also exhibits a rich lithium insertion chemistry, typically cycling at slightly lower potentials than the spinel at 1.35 V. Although the electrochemistry of the series of titanium oxide and the lithium titanate materials is very interesting, the working potential of around 1.5 V_{Li} means that they are optimal for neither positive nor negative electrode material in high-voltage, rechargeable lithium-ion batteries.

$H_2Ti_3O_7$ with ramsdellite structure type was previously shown to exhibit attractive conductivities, 2.66×10^{-6} S cm^{-1} at 200 °C, most likely due to protonic transport, which suggests a potential application of hydrogen-form titanates as fuel cell electrolytes in protonic fuel cells.[18] Conductivity measurements on nanotubular $H_2Ti_3O_7 \cdot 0.8H_2O_{abs}$ indicate that mainly protonic transport occurs at temperatures below 150 °C and that the proton conductivity is ca. 5.5×10^{-6} S cm^{-1} at 30 °C.[19] Mesoporous monocrystalline TiO_2 may show interesting properties because of their large surface area.

Porous TiO_2 materials with amorphous or polycrystalline walls have been previously synthesized using soft templates.[20,21] Lithium insertion in anatase TiO_2 has been extensively studied and has been achieved to a high level corresponding to $Li_{0.5}TiO_2$. A recent work demonstrated that porous polycrystalline rutile TiO_2 can accommodate more Li, $Li_{0.7}TiO_2$, during the first discharge, showing high potential application as an anode material.[20] It is interesting to see whether mesoporous monocrystalline rutile TiO_2 can accommodate even more lithium ions because of its high tolerance to volume change.[22] In our attempts at synthesizing such materials, we had to face several difficulties. For example, at high temperature, TiO_2 crystals may react with amorphous silica wall forming Ti−O−Si bonds, leading to a deposition of either layers or nanoparticles of TiO_2 instead of porous crystals.[23] For low-temperature crystallization, a suitable titanium precursor with a low melting point should be used, e.g., nitrates are commonly used as precursors for fabricating many mesoporous metal oxides. However, titanium nitrates are unstable and are not commercially available. It has been also noticed that, at low temperatures, anatase phase rather than rutile phase of TiO_2 is normally produced.

Herein is reported our successful synthesis of ordered mesoporous rutile TiO_2 templated by SBA-15 and KIT-6, using freshly prepared titanium nitrate solution as a precursor. Some physicochemical properties of the new products, e.g., proton conductivity and Li-ion insertion, were also investigated to demonstrate their application potential.

Experimental Section

Mesoporous silicas SBA-15 and KIT-6 were synthesized according to the published literature.[4,5] A titanium source, such as titanium isopropoxide ($Ti[OCH(CH_3)_2]_4$) or tetrabutyl titanate ($Ti[OC_4H_9]_4$), was dissolved in ethanol under stirring and distilled water was added dropwise into the solution until no more white precipitate of titanium hydroxide was produced. The white precipitate was recovered by filtering and washing with distilled water. After drying, 0.2 g of the precipitate was dissolved in 20 mL HNO_3 (70%) solution to form a 0.085 M titanium nitrate solution (calculated based on Ti ions).[24] Subsequently, 0.15 g of SBA-15 or KIT-6 was mixed with the titanium nitrate solution under stirring for 2 h, and the mixed solution (the ratio of contents is 1.7 mmol Ti^{4+}:20 mL 70% HNO_3 solution:0.15 g SBA-15) was transferred into a 50 mL crucible and dried at 40 °C. The dried white powder was placed in a muffle furnace for calcination. HNO_3 was in excess in this starting suspension and it was expected that about 25% total pore volume in SBA-15 would be filled by TiO_2 in the TiO_2/silica

---

(13) (a) Yue, W. B.; Hill, A. H.; Harrison, A.; Zhou, W. Z. *Chem. Commun.* **2007**, 2518–2520. (b) Yue, W. B.; Zhou, W. Z. *J. Mater. Chem.* **2007**, *17*, 4947–4952.

(14) (a) Pavasupree, S.; Ngamsinlapasathian, S.; Nakajima, M.; Suzuki, Y.; Yoshikawa, S. *J. Photochem. Photobiol., A* **2006**, *184*, 163–169. (b) Pavasupree, S.; Jitputti, J.; Ngamsinlapasathian, S.; Yoshikawa, S. *Mater. Res. Bull.* **2008**, *43*, 149–154. (c) Yu, C. Y.; Hyodo, T.; Shimizu, Y.; Egashira, M. *Electrochemistry* **2003**, *71*, 475–480. (d) Guo, Y. G.; Hu, Y. S.; Sigle, W.; Maier, J. *Adv. Mater.* **2007**, *19*, 2087–2091.

(15) (a) von Oertzen, G. U.; Gerson, A. R. *J. Phys. Chem. Solids* **2007**, *68*, 324–330. (b) Reddy, M. A.; Kishore, M. S.; Pralong, V.; Caignaert, V.; Varadaraju, U. V.; Raveau, B. *Electrochem. Commun.* **2006**, *8*, 1299–1303. (c) Murphy, D. W.; Cava, R. J.; Zahurak, S. M.; Santoro, A. *Solid State Ionics* **1983**, *9−10*, 413–417. (d) Gover, R. K. B.; Tolchard, J. R.; Irvine, J. T. S.; Murai, T.; Tukamoto, H. *J. Electrochem. Soc.* **1999**, *146*, 4348–4353. (e) Tsuyumoto, I.; Uchikawa, H. *Mater. Res. Bull.* **2004**, *39*, 1737–1744. (f) Kuhn, A.; Amandi, R.; Garcia-Alvarado, F. *J. Power Sources* **2001**, *92*, 221–227. (g) Noailles, L. D.; Johnson, C. S.; Vaughey, J. T.; Thackeray, M. M. *J. Power Sources* **1999**, *81−82*, 259–263.

(16) (a) Deschanvres, A.; Raveau, B.; Sekkal, Z. *Mater. Res. Bull.* **1971**, *6*, 699–704. (b) Bach, S.; Pereira-Ramos, J. P.; Baffier, N. *J. Mater. Chem.* **1998**, *8*, 251–253.

(17) Gover, R. K. B.; Irvine, J. T. S. *J. Solid State Chem.* **1998**, *141*, 365–372.

(18) Corcoran, D. J. D.; Tunstall, D. P.; Irvine, J. T. S. *Solid State Ionics* **2000**, *136−137*, 297–303.

(19) Thorne, A.; Kruth, A.; Tunstall, D.; Irvine, J. T. S.; Zhou, W. Z. *J. Phys. Chem. B* **2005**, *109*, 5439–5444.

(20) Wang, D.; Choi, D.; Yang, Z.; Viswanathan, V. V.; Nie, Z.; Wang, C.; Song, Y.; Zhang, J.-G.; Liu, J. *Chem. Mater.* **2008**, *20*, 3435–3442.

(21) (a) Grosso, D.; Soler-Illia, G. J. A. A.; Babonneau, F.; Sanchez, C.; Albouy, P. A.; Brunet-Bruneau, A.; Balkenende, A. R. *Adv. Mater.* **2001**, *13*, 1085–1090. (b) Tian, B. Z.; Yang, H. F.; Liu, X. Y.; Xie, S. H.; Yu, C. Z.; Fan, J.; Tu, B.; Zhao, D. Y. *Chem. Commun.* **2002**, 1824–1825. (c) Dong, W. Y.; Sun, Y. J.; Lee, C. W.; Hua, W. M.; Lu, X. C.; Shi, Y. F.; Zhang, S. C.; Chen, J. M.; Zhao, D. Y. *J. Am. Chem. Soc.* **2007**, *129*, 13894–13904.

(22) Dupont, L.; Laruelle, S.; Grugeon, S.; Dickinson, C.; Zhou, W. Z.; Tarascon, J.-M. *J. Power Sources* **2008**, *175*, 502–509.

(23) (a) Perathoner, S.; Lanzafame, P.; Passalacqua, R.; Centi, G.; Schlogl, R.; Su, D. S. *Microporous Mesoporous Mater.* **2006**, *90*, 347–361. (b) Wang, Z. Y.; Zhang, F. X.; Yang, Y. L.; Xue, B.; Cui, J.; Guan, N. J. *Chem. Mater.* **2007**, *19*, 3286–3293. (c) Wang, W.; Song, M. *Microporous Mesoporous Mater.* **2006**, *96*, 255–261. (d) Grieken, R. V.; Aguado, J.; Lopez-Munoz, M. J.; Marugan, J. *J. Photochem. Photobiol., A* **2002**, *148*, 315–322.

(24) (a) Liu, X. H.; Yang, J.; Wang, L.; Yang, X. J.; Lu, L. D.; Wang, X. *Mater. Sci. Eng., A* **2000**, *289*, 241–245. (b) Wang, C. M.; Wu, H.; Chung, S. L. *J. Porous Mater.* **2006**, *13*, 307–314.

product. Temperature was increased from room temperature up to 100, 200, 300, 400, and 600 °C with a rate of 1 °C/min, and the specimens were kept at the terminal temperatures for 5 h before being cooled down to room temperature. The as-made TiO_2/silica composite was mixed with 0.2 M NaOH solution at 80 °C by stirring for 2−3 min, and the suspension was centrifuged to recover TiO_2. This process was repeated once again. The TiO_2 powder was washed with distilled water twice, followed by drying at 40 °C, and assigned TiO_2(S)-T, where S is a name of silica template and T is the calcination temperature. Mesoporous silicas FDU-12[6] and SBA-16[7] were also used as hard templates to prepare porous TiO_2 particles, and the treated products after calcination at 300 °C were labeled TiO_2(FDU-12)-300 and TiO_2(SBA-16)-300, respectively. The silica template was removed by stirring the specimen in 0.2 M NaOH solution for 3 min.

The conductivity of the mesoporous TiO_2 was examined by a.c. impedance spectroscopy. Pellets were used and obtained by pressing the powder TiO_2 under 1×10^3 kg/cm^2. PTFE bonded carbon black (Carbot Vulcan 72R) and carbon paper (Torory TGPH-090) were used as electrodes and current collector respectively. The whole assembly was then mounted in tube furnaces with temperature and humidity carefully adjusted.

For electrochemical characterization, electrode materials were prepared as “Bellcore” type electrodes, and assembled into coin cells, as previously described.[25] A slurry was made by grinding 11.6 wt % dry active material and 1.4 wt % Super S carbon together and then adding 5.5 wt % polyvinylidene fluoride (PVDF), 9.5 wt % propylene carbonate (PC), and 72 wt % acetone. The slurry was stirred for 4 h in a 50 °C water bath and then doctor bladed onto a glass plate, to form a self-supporting sheet, typically 100−200 μm thick after evaporation of the acetone. The electrode sheet was cut into discs, and the trapped (PC) was leached out using ether, until the individual electrodes reached constant weight. The resulting porous electrodes were dried under a vacuum and transferred to an argon-filled glovebox. A MacPile (Biologic) battery testing system was used to collect the electrochemical data. Galvanostatic cycling was recorded between set potential limits, typically 0.8 and 3.5 V, after the first reduction sweep. There was one hour relaxation time at the end points. Potentiostatic data were recorded with 1 h relaxation time at the end points (typically 0.8 and 3.5 V with a step rate of 20 mV/h).

TGA measurement of titanium-loaded KIT-6 was performed on Perkin-Elmer TGA/DTA. The products synthesized at various temperature were initially characterized using X-ray powder diffraction (XRD) on a Philips reflective diffractometer with Cu Kα radiation ($\lambda = 0.1542$ nm). Further structural investigation was performed using transmission electron microscopy (TEM) and high-resolution TEM (HRTEM) on a JEOL JEM-2011 electron microscope operated at 200 kV. Energy-dispersive X-ray microanalysis (EDX) attached in electron microscope was used to qualitatively determine the present elements. Selected area electron diffraction (SAED) was used to determine the crystallinity of the materials and to identify the crystallographic systems. A micromeritics instrument ASAP 2020 was used to examine the N_2 adsorption and desorption properties of the mesoporous metal oxides at 77 K. Specific surface areas were calculated via the Brunauer−Emmett−Teller (BET) model, and pore size distribution graphs were obtained from the non-local density functional theory (NLDFT) model.

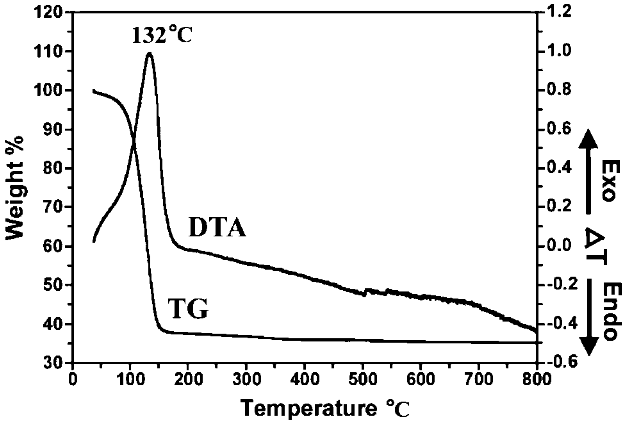

Figure 1. TG/DTA curves of titanium-loaded KIT-6 specimen.

Results and Discussion

TGA investigation of a titanium-loaded KIT-6 specimen was performed with an air flow rate of 35 mL/min and a heating rate of 5 °C /min, showing a single peak of weight loss, from ca. 36 to ∼150 °C (Figure 1). In this region, water evaporation and decomposition of HNO_3, titanium nitrate, and titanium oxide hydroxide are expected.[23] The corresponding DTA curve shows one exothermic peak at 132 °C. There was no further weight loss when temperature was increased from 150 to 800 °C, implying a final crystalline product of pure TiO_2 and a possible low crystallization temperature (<150 °C) of TiO_2.

The crystal phase and mesostructure of porous TiO_2 highly depended on the reaction temperature. From XRD patterns of mesoporous TiO_2 templated by KIT-6 for both small-angle and wide-angle regions (Figure 2), the characteristic diffraction peaks of the mesostructure in Figure 2a can be observed at about 0.86°, indexed as the (211) reflection of the KIT-6 like mesostructure, which is cubic, space group $Ia\bar{3}d$. The unit-cell parameters of all the observed mesostructures calculated from the (211) peaks are similar, ∼25.1 nm, which is close to the value obtained from the TEM images (24.8 nm) in Figure 3.

Figure 2b indicates that rutile rather than anatase phase starts to appear at a low temperature (100 °C). The intensities and sharpness of the diffraction peaks increase with the reaction temperature, and the rutile phase is the only phase (<200 °C) or principle phase (>300 °C) in all the samples. The anatase TiO_2 phase was detected from the specimens prepared at high temperature. Two weak diffraction peaks of anatase, (101) and (200), are observed from the products prepared at 300 °C and above (Figure 2b). The percentage of the anatase is low in all the samples (<5%). Bearing in mind that Shi et al. produced rutile TiO_2 powder by a hydrolysis method in a HNO_3 solution at low temperatures (80 °C or lower), but pure anatase TiO_2 was obtained at a slightly higher temperature (e.g., 100 °C),[26] the formation of rutile TiO_2 at a large temperature range from 100 to 600 °C using KIT-6 as a template can probably be attributed to a confinement effect of the mesopores, in which a phase transformation from high-density rutile (4.23 g/cm^3) to low-

---

(25) Connor, P. A.; Belliard, F.; Behm, M.; Tovar, L. G.; Irvine, J. T. S. *Ionics* **2002**, *8*, 172–176.

(26) Shi, L. J.; Yang, R.; Li, M.; Chin, J. *Inorg. Chem.* **2006**, *22*, 1196–1202.

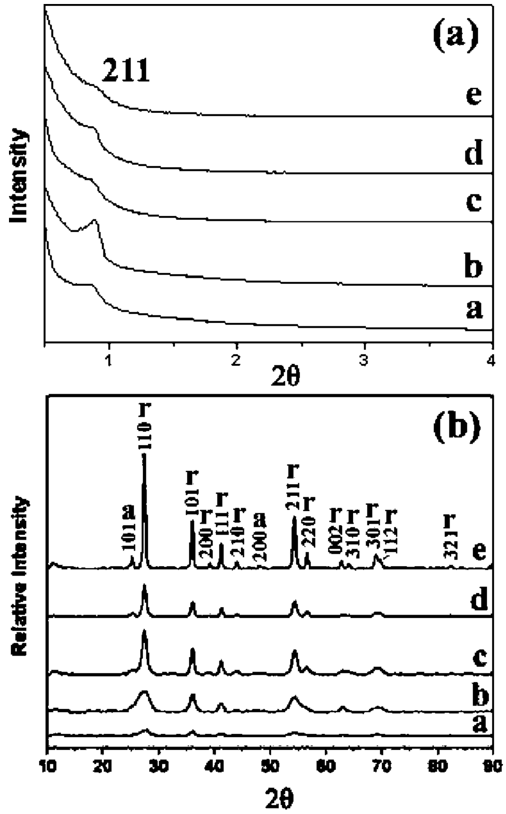

Figure 2. XRD patterns of porous TiO$_2$ crystals templated by KIT-6 in (a) small-angle and (b) wide-angle regions. The peaks in (b) are indexed onto the tetragonal rutile phase with $a = 0.4600$ nm, $c = 0.2965$ nm, marked by **r**, and two small peaks indexed to the tetragonal anatase phase with $a = 0.3785$ nm, $c = 0.9514$ nm, marked by **a**. The specimens are labeled, a, TiO$_2$(KIT-6)-100; b, TiO$_2$(KIT-6)-200; c, TiO$_2$(KIT-6)-300; d, TiO$_2$(KIT-6)-400; and e, TiO$_2$(KIT-6)-600.

density anatase (3.90 g/cm^3)[27] is suppressed. Another possible factor that is even more important is the special precursor of titanium nitrate complex used with a high concentration of (NO$_3$)$^-$, which is discussed below.

The TiO$_2$ products synthesized at various thermal stages are all mesoporous crystals and have replicated structure of SBA-15 or KIT-6. Images a and b in Figure 3 show TEM images of (a) TiO$_2$(SBA-15)-200 and (b) TiO$_2$(SBA-15)-300 specimens, viewed down the [001] and [110] axes of the SBA-15 like mesostructure. The porous particles have a hexagonal arrangement of nanorod arrays connected by small nanobridges, consistent with the expected morphology of replicas of SBA-15 (see the Supporting Information, Figure S1a). Images c and d in Figure 3 are TEM images from (c) TiO$_2$(KIT-6)-200 and (d) TiO$_2$(KIT-6)-300 specimens, viewed down the [531] and [111] zone axes of the KIT-6 like mesostructure, respectively. It was observed that the particles have a highly ordered pore network, a large average size of about 650 nm and irregular shapes as shown in Figure 3d. The TEM image contrast patterns also indicate that the whole bicontinuous channel network in KIT-6 has been replicated, unlike KIT-6 templated porous Cr$_2$O$_3$, where only half of the channel system can be replicated. The key factor, as discussed previously,[9] is most likely the low calcination temperature, which allows the small channels connecting the main channels to be well-maintained.

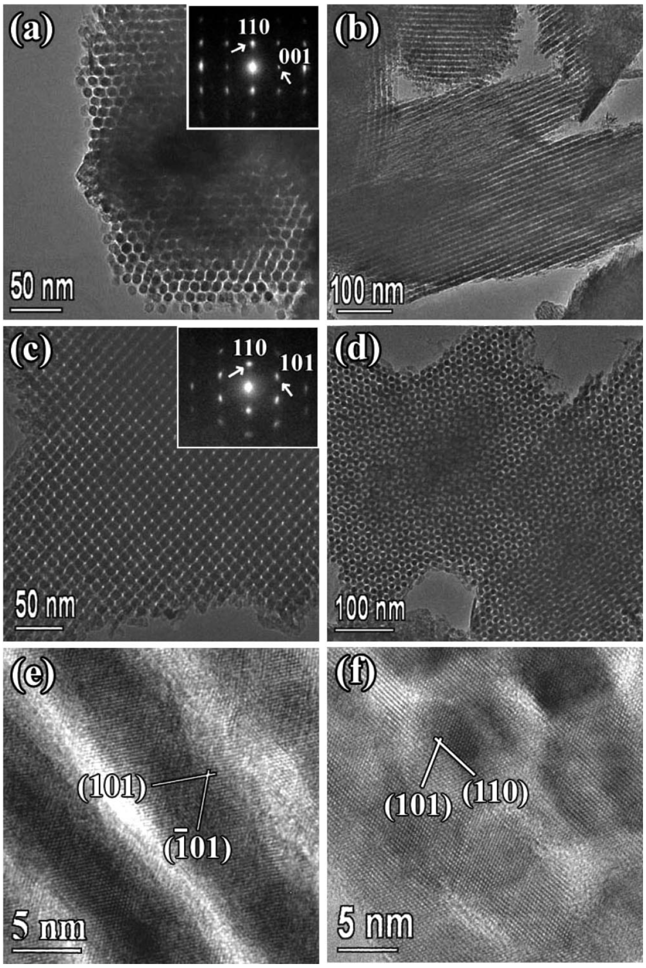

Figure 3. TEM images of mesoporous (a) TiO$_2$(SBA-15)-200, (b) TiO$_2$(SBA-15)-300, (c) TiO$_2$(KIT-6)-200, and (d) TiO$_2$(KIT-6)-300; and HRTEM images of (e) TiO$_2$(SBA-15)-600 and (f) TiO$_2$(KIT-6)-600. The insets of a and c are the SAED patterns, indexed to the rutile structure. The *d*-spacings of the marked fringes in e are ca. 0.249 and 0.249 nm, corresponding to the (101) and ($\bar{1}$01) planes, and those in f are ca. 0.249 and 0.325 nm, corresponding to the (101) and (110) planes of rutile TiO$_2$, respectively.

SAED from both SBA-15 and KIT-6 templated particles gave single-crystal patterns. For example, the insets in images a and c in Figure 3 can be indexed to tetragonal rutile structure with the view directions of [$\bar{1}$10] and [$\bar{1}$11]. HRTEM images also confirm that the mesoporous particles are rutile-type monocrystalline. The separated nanorods in Figure 3e have uniform crystal orientation. In Figure 3f, the crystal orientations of all the nanoparticles are the same. The space between the nanorods forms a mesopore network.

The chemical compositions of the products were examined by using EDX. A small amount of Si was observed in the products (see the Supporting Information, Figure S2a), an average atomic ratio of Si/Ti, 3.1 ± 0.4%, from 22 randomly selected particles, indicating that the residual SiO$_2$ is possibly attributed to a formation of Si−O−Ti bonds on the surface of the TiO$_2$ crystals, which can not be removed completely by a dilute (0.2 M) NaOH solution. This impurity of Si does not introduce any notable changes in the rutile crystal structure. When a 2 M NaOH solution was used for a long washing time (e.g. 6−18 h), Si was completely removed (see

---

[27] Masahashi, N. *Mater. Sci. Eng., A* **2007**, *452−453*, 721–726.

the Supporting Information, Figure S2b). However, in this case, the surface of TiO_2 particles was eroded and the ordered mesostructure was partially destroyed (see the Supporting Information, Figure S3). It is believed that the very low level of silicon in the porous TiO_2 normally does not affect the physicochemical properties of the porous crystals. In proton conductivity, these surface Ti−O−Si functional groups may even enhance the conductivity.

Mesoporous silica FDU-12 or SBA-16 consists of spherical nanocavities linked together by small nanochannels. However, the mesostructures and crystallinities of TiO_2 templated by these mesoporous silicas, e.g., TiO_2(FDU-12)-300 and TiO_2(SBA-16)-300, are poor. According to our previous work,[13] only metal oxides with a cubic structure, such as Co_3O_4 and In_2O_3, can form porous crystals in the FDU-12 and SBA-16 templates. Anisotropic crystal growth of non-cubic metal oxides inside the spherical cages of FDU-12 or SBA-16 would lead to a distortion of the silica framework, resulting in blockage of the intercage channels. Rutile TiO_2 has a tetragonal structure and therefore the unsuccessful synthesis of porous TiO_2 in FDU-12 and SBA-16 further confirms our previous speculation.

Porosities and pore sizes of the porous TiO_2 products templated by SBA-15 and KIT-6 were also examined. N_2 adsorption/desorption isotherms of the TiO_2(KIT-6)-T specimens show a type IV curve with a hysteresis loop, indicating a mesopore feature as shown in Figure 4a. Figure 4b shows the derived pore size distributions. The specific surface areas, pore sizes, and pore volumes of the porous TiO_2 crystals are displayed in Table 1.

General speaking, a wide pore size distribution is expected from these porous crystals because the pore shapes, negative replicas of the wall of the silica templates, are complicated. However, it is still worth comparing the pore size distributions of the samples prepared at different temperatures. It is noted that the pore size distributions of the specimens prepared at low temperatures are narrower and the corresponding peak position increases from 4.9 nm in TiO_2(KIT-6)−100 to 7.2 nm in TiO_2(KIT-6)-600. This remarkable change is due to the density variation of the TiO_2 crystals, i.e., the crystals would shrink at a high temperature, leaving relatively larger space. The effect of contraction to the quality of titania mesostructure is not simple. There are two types of contraction involved. One takes place during the decomposition of the precursor and the formation of TiO_2. The another is related to the microstructure of TiO_2 or the crystallinity of the oxide as mentioned above. High temperature can normally help to produce a high density oxide, which contains fewer defects. However, too fast decomposition of the precursor in the template pores at a high temperature leads to many disconnections of the crystals, and therefore a poor mesostructure. The yield of porous TiO_2 crystals was reduced when a high temperature was applied. It is noted that some very large pores may exist in the samples prepared at high temperatures, e.g., the broad peaks marked by 14.4 and 22.3 nm in Figure 4b. These could be attributed to the space between nonporous TiO_2 nanoparticles, the percentage of these particles increases with the calcination temperature. The surface areas of mesoporous TiO_2 range from 44.9 to 130 m^2/g, with the largest value observed from TiO_2(KIT-6)-200, also listed in Table 1.

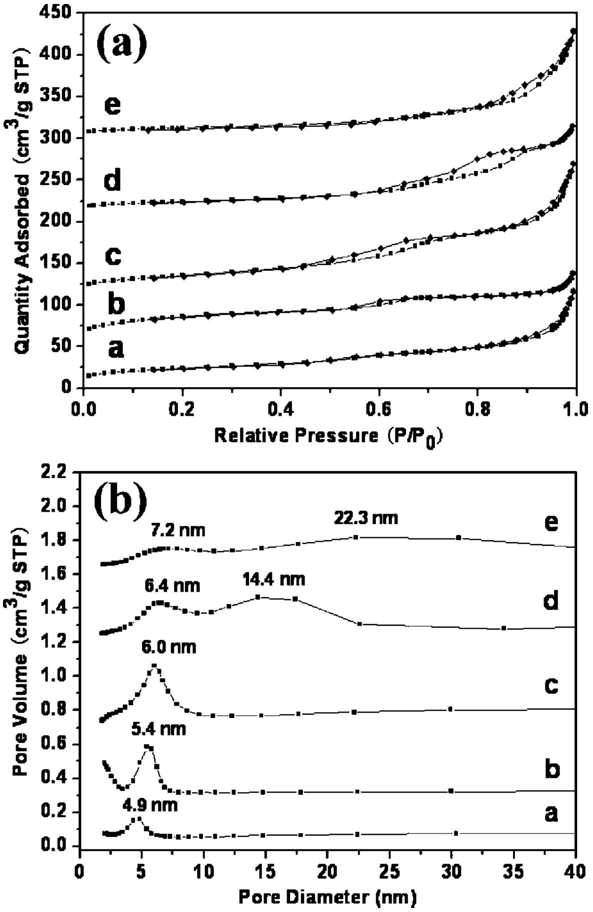

Figure 4. (a) Nitrogen adsorption/desorption isotherms measured at 77 K from porous crystals of TiO_2 templated by KIT-6. (b) Pore size distributions of the corresponding specimens with synthetic temperature a, 100; b, 200; c, 300; d, 400; and e, 600 °C.

Table 1. Pore Size (*D*), Pore Volume (*V*), Surface Area Per Unit Weight (S_w) and Per Unit Volume (S_v) of Template KIT-6 and KIT-6 Templated TiO_2 from BET Measurements

sample	*T* (°C)[a]	*D* (nm)	*V* (cm^3/g)	S_w (m^2/g)	S_v (m^2/cm^3)
KIT-6	550	10.1	0.97	810	568
TiO_2-100	100	4.9	0.18	86.8	208
TiO_2-200	200	5.4	0.14	130	346
TiO_2-300	300	6.0	0.25	91.2	188
TiO_2-400	400	6.4	0.16	50.6	128
TiO_2-600	600	7.2	0.20	44.9	103

[a] *T* = calcination temperature.

Figure 5a presents the change in conductivity of pressed pellets of porous TiO_2(KIT-6)-200 and conventional rutile powder on heating in air from room temperature to 100 °C. The values were obtained from a.c. impedance spectra at the low-frequency intercept of the electrode processes (see the Supporting Information, Figure S4) with the real axis and so is a combination of grain and intergrain contributions. It is reasonable to assume that this conductivity is related to adsorbed water in the intergrain regions. It was not reversible on cooling as the water lost on heating was not readily replaced on cooling and is likely to be protonic in nature. It is important to note that the conductivity of the mesoporous sample is much higher and persists to higher temperature

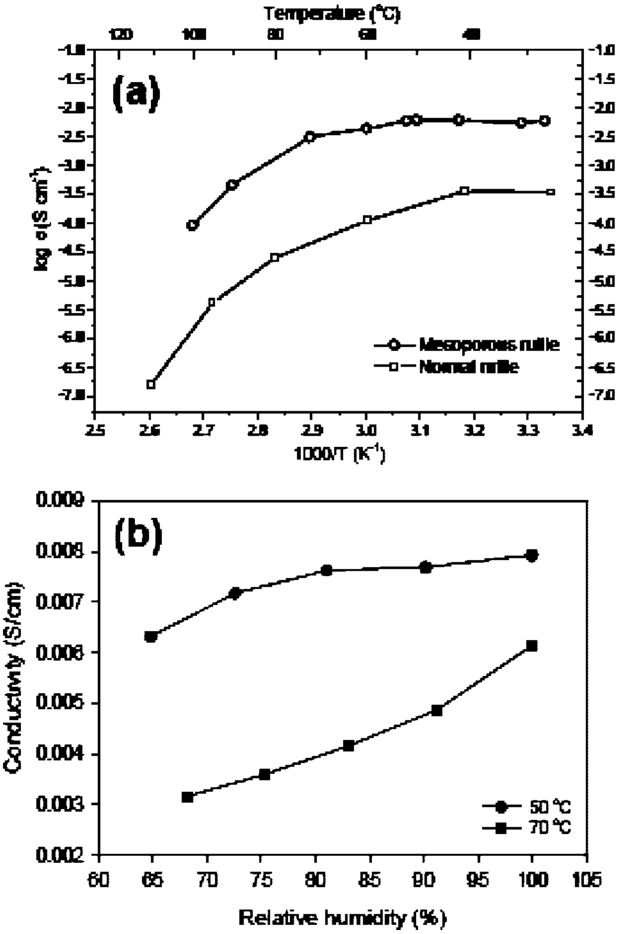

Figure 5. (a) Conductivity in air vs temperature of porous rutile TiO_2(KIT-6)-200 and normal rutile @3% RH and (b) conductivity of TiO_2(KIT-6)-200 vs relative humidity at 50 and 70 °C.

than the conventional material, due of course to the high internal surface area.

The conductivity dependence upon relative humidity (RH) was also evaluated, equilibrating at each RH for 1 h, and is shown in Figure 5b. Mesoporous TiO_2 presented a higher conductivity at 50 °C than that at 70 °C in the RH from 60 to 100%. The highest conductivity 8×10^{-3} S cm^{-1} was obtained at 50 °C under 100% RH.

Electrodes made from dried TiO_2(KIT-6)-200 were tested in both potentiostatic and galvanostatic mode. In the controlled potential scan, the electrode was cycled over a voltage window of 0.8 to 3.5 V_{Li} (Figure 6a). In the initial part of the cycle from open circuit voltage to 1.6 V, a small broad peak can be observed that is ascribed to initial partial reduction of Ti^{4+}. A very typical reduction peak is observed at around 1.5 V as has previously been observed for two phase equilibria in lithium titanate spinel or ramsdellite reductions. The second main peak at 1.09 V_{Li} of an unusually low potential is observed for a titanate reduction, but would lead to significantly higher potential if utilized as a negative electrode in a lithium ion battery. A much broader peak is observed on the reverse scan at almost 2 V_{Li}, which cycles reversibly with a broad peak at 1.8 V_{Li}. This change in form probably indicates disruption of the mesoporous titanate on Li insertion to 1 V.

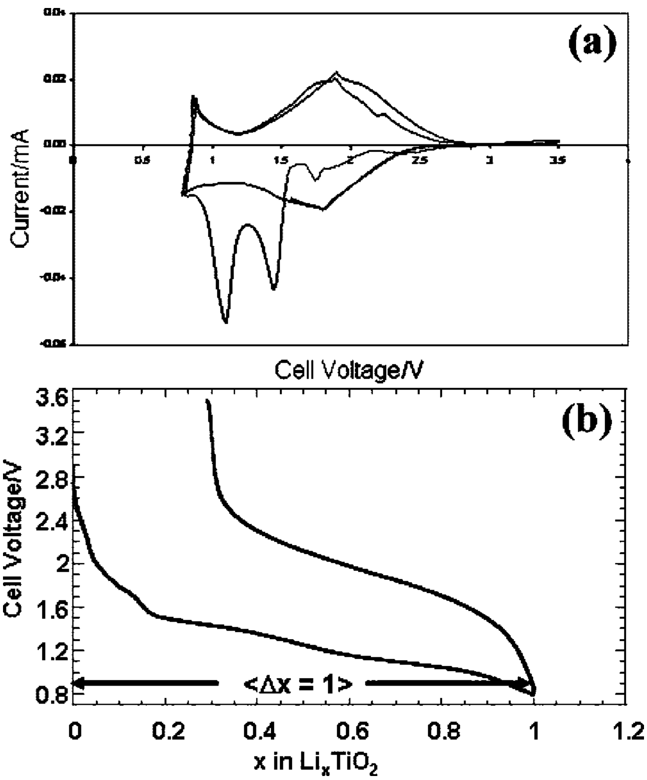

Figure 6. (a) Potentiostic plot of TiO_2(KIT-6)-200 in a voltage window of [0.8, 3.5 V_{Li}] with a scan rate of ±20 mV/h. Total $x = 1$ inserted at 0.8 V. (b) Galvanostatic plot of TiO_2 in a voltage window of [0.8, 3.5 V_{Li}].

The capacity associated with the initial cycle indicated by the data obtained galvanostatically (Figure 6b) is 1 Li^+ per TiO_2 unit for the first discharge sweep that corresponds to 335 mA h/g (the theoretical specific capacity of TiO_2 polymorphs of anatase, rutile, TiO_2(B), etc.). On the second sweep related to the first charge, 0.71 Li^+ per TiO_2 was extracted, leading to a nominal reversible capacity of 270 mA h/g. This good performance on first cycle is presumably due to the high surface area and high crystallinity of this mesoporous rutile TiO_2.

In contrast to the previously prepared titania-containing SBA-15,[22,28] the Ti-source used in the present work was isopropoxide. However, after the hydrolysis, treatment of excess nitrate acid and drying process as described in the Experimental Section, the real precursor, which moves into the template pores, was a titanium nitrate complex. The long Ti−O−Ti chains in titanium oxynitrate, which is the hydrolysate of titanium nitrate by partially losing HNO_3 during drying and thermal treatment (see the Supporting Information, Figure S5), ensure a high loading of the precursor to form large TiO_2 crystals inside the KIT-6 pores instead of forming separated nanocrystallites or a layer of TiO_2 on the inner walls of silica.[29] The presence of nitrate anions is also important in the selective formation of rutile instead of anatase. It has been previously reported[26,30,31] that

---

(28) Ohno, T.; Haga, D.; Fujihara, K.; Kaizaki, K.; Matsumura, M. *J. Phys. Chem. B* **1997**, *101*, 6415–6419.

(29) Vradman, L.; Landau, M. V.; Kantorovich, D.; Koltypin, Y.; Gedanken, A. *Microporous Mesoporous Mater.* **2005**, *79*, 307–318.

(30) Wang, C. C.; Ying, J. Y. *Chem. Mater.* **1999**, *11*, 3113–3120.

(31) Yin, H. B.; Wada, Y.; Kitamura, T.; Kambe, S.; Murasawa, S.; Mori, H.; Sakata, T.; Yanagida, S. *J. Mater. Chem.* **2001**, *11*, 1694–1703.

rutile TiO_2 can form from amorphous TiO_2 in the presence of HNO_3 in an acidic condition. The possible effect of HNO_3 is as follows. One of the most important structural differences in between rutile and anatase is that the former contains edge-sharing $[TiO_6]$ octahedra but the latter forms by face-sharing $[TiO_6]$ octahedra. Titanium exists in the form of a 6-fold coordinated hydrated ion $[Ti(H_2O)_6]^{4+}$ rather than Ti^{4+} cation in a solution and finally the $[TiO_6]$ octahedra are formed by olation and oxolation. The use of excess HNO_3 leads to a high degree protonation of the $[TiO_6]$ octahedra, forming $[(H_2O)_5Ti\text{-}(OH)]^{3+}$, whereas NO_3^- anions have a weaker affinity for titanium ions. These $[(H_2O)_5Ti\text{-}(OH)]^{3+}$ ions share edges through olation, forming a linear chain polymer. This edge-sharing structural feature has a closer relation with rutile rather than anatase.[26,31,32]

On the other hand, anatase TiO_2 is possibly a product of decomposition of $TiO(NO_3)_2$ when a large amount of NO_3^- anions in the system have been removed at a high temperature (>200 °C). The percentage of anatase TiO_2 increases when the content of HNO_3 is reduced. To confirm this effect, we prepared another specimen, TiO_2(d-HNO_3)-200, with a dilute HNO_3 solution, and the percentage of the anatase phase increased significantly (Figure 7). Because porous anatase has not been observed by TEM, the formed anatase will reduce the yield of porous TiO_2 (rutile). To fully understand the mechanism of this effect of nitrate ions, more investigations will have to be carried out, including more detailed studies of microsctructures of mixed phase of rutile and anatase.

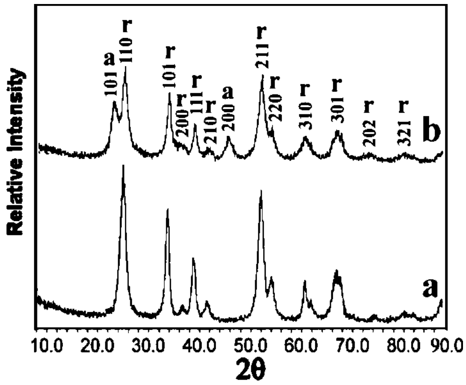

Figure 7. XRD patterns of porous TiO_2: (a) TiO_2(KIT-6)-200 and (b) TiO_2(d-HNO_3)-200.

Conclusions

Mesoporous rutile TiO_2 crystals with high surface areas have been fabricated using mesoporous silicas, SBA-15 and KIT-6, as hard templates. The present work demonstrates a novel low-temperature synthesis of porous rutile TiO_2. Mesoporous TiO_2 with mixed phases of rutile and anatase can also be produced and the proportion of anatase can be tuned by the calcination temperature and the concentration of HNO_3. The proton conductivity of mesoporous rutile TiO_2 templated by KIT-6 was found to be quite high at high relative humidity at temperatures of 50 °C compared to normal rutile and such mesoporous materials might be useful as inorganic fillers in proton exchange membranes. The new materials also show promising Li^+ insertion potentials. However, the structure seems to be disrupted on Li^+-insertion losing this attractive redox chemistry at 1 V. Further exploration of the insertion chemistry and doping of the TiO_2 to examine the possibility of retaining the low potential step on cycling would be worthwhile.

Acknowledgment. W.Z. thanks St. Andrews University for an EaStCHEM studentship for W.Y. J.T.S.I. thanks EPSRC for Platform and Senior Fellowship support. H.Y.H. and D.Y.Z. thank NSF of China for financial support.

Supporting Information Available: Morphology of porous TiO_2 products, EDX spectra, TEM images of specimens washed with 2 M NaOH, A.C. impedance spectrum, schematic drawing of Ti−O−Ti chains (PDF). This material is available free of charge via the Internet at http://pubs.acs.org.

CM900197P

---

(32) Li, Y.; White, T. J.; Lim, S. H. *J. Solid State Chem.* **2004**, *177*, 1372–1381.